Mesoporous Co_3O_4 and CoO@C Topotactically Transformed from Chrysanthemum-Like $Co(CO_3)_{0.5}(OH)\cdot 0.11H_2O$ and Their Lithium-Storage Properties

*Shenglin Xiong, Jun Song Chen, Xiong Wen Lou, and Hua Chun Zeng**

In this work, a novel hydrothermal route is developed to synthesize cobalt carbonate hydroxide, $Co(CO_3)_{0.5}(OH)\cdot 0.11H_2O$. In this method, sodium chloride salt is utilized to organize single-crystalline nanowires into a chrysanthemum-like hierarchical assembly. The morphological evolution process of this organized product is investigated by examining different reaction intermediates during the synthesis. The growth and thus the final assembly of the $Co(CO_3)_{0.5}(OH)\cdot 0.11H_2O$ can be finely tuned by selecting preparative parameters, such as the molar ratio of the starting chemicals, the additives, the reaction time and the temperature. Using the flower-like $Co(CO_3)_{0.5}(OH)\cdot 0.11H_2O$ as a solid precursor, quasi-single-crystalline mesoporous Co_3O_4 nanowire arrays are prepared via thermal decomposition in air. Furthermore, carbon can be added onto the spinel oxide by a chemical-vapor-deposition method using acetylene, which leads to the generation of carbon-sheathed CoO nanowire arrays (CoO@C). Through comparing and analyzing the crystal structures, the resultant products and their high crystallinity can be explained by a sequential topotactic transformation of the respective precursors. The electrochemical performances of the typical cobalt oxide products are also evaluated. It is demonstrated that tuning of the surface texture and the pore size of the Co_3O_4 products is very important in lithium-ion-battery applications. The carbon-decorated CoO nanowire arrays exhibit an excellent cyclic performance with nearly 100% capacity retention in a testing range of 70 cycles. Therefore, this CoO@C nanocomposite can be considered to be an attractive candidate as an anode material for further investigation.

1. Introduction

In recent years, porous inorganic materials have received significant attention in the materials-research community owing to their promising applications across various fields, such as lithium-ion batteries,[1,2] ion exchange[3] and catalytic processes,[4,5] because of their ability to interact with ions, atoms and molecules, not only on the surface or at the interface, but also throughout the bulk phase of materials.[6] Among many preparative methods for this class of materials, in particular, the transformation of materials of interest from a conventional continuous solid phase to a nanostructured porous phase provides a useful strategy for improving their performance. As important transition-metal oxide semiconductors, divalent cobalt oxide, CoO, with an optical band gap at 2.4 eV,[7] and mixed-valent spinel cobalt oxide, Co_3O_4, with direct optical band gaps at 1.48 and 2.19 eV,[7] have undergone extensive investigation in recent years in view of their wide-ranging potential applications as gas sensors,[8,9] heterogeneous catalysts,[10] magnetic materials,[11] solar-energy absorbers,[12] supercapacitors[13] and rechargeable lithium-ion-battery (LIB) materials.[14–27] More importantly, due to its high theoretical capacity, nanostructured Co_3O_4 (similarly CoO) is widely considered to be an attractive anode material for next-generation lithium-ion batteries. Nevertheless, it should be pointed out that the application of cobalt oxides in practical LIBs is seriously hindered by their relatively large initial irreversible loss and poor capacity retention over extended cycling. These problems could partly originate from the large volume change during the insertion and deinsertion cycles of the lithium ions, which causes a disintegration of the battery material and a loss of electrical contact, eventually leading to permanent electrode failure. Another contributing factor could be the formation of a solid electrolyte interface (SEI), which has been ascribed commonly to side reactions such as reductive decomposition of the electrolyte.[28] Therefore, considerable research effort has been directed to the design and synthesis of new nanostructured cobalt oxides with enhanced technological performance.[8–34]

Up until now, a variety of synthetic protocols have been developed to prepare cobalt-based oxides with different morphologies and desired micro- and nanostructures. Among them, a two-step strategy has generated huge interest and is widely practiced, wherein cobalt-containing solid precursors

Dr. S. L. Xiong, Prof. H. C. Zeng
Department of Chemical and Biomolecular Engineering
KAUST-NUS GCR Program
Faculty of Engineering
National University of Singapore
10 Kent Ridge Crescent, Singapore 119260, Singapore
E-mail: chezhc@nus.edu.sg
Dr. J. S. Chen, Prof. X. W. Lou
School of Chemical and Biomedical Engineering
Nanyang Technological University
70 Nanyang Drive, Singapore 637457, Singapore

DOI: 10.1002/adfm.201102192

(i.e., cobalt hydroxide, cobalt nitrate hydroxide, cobalt nitrate carbonate hydroxide, cobalt hydroxyoxide, and cobalt carbonate etc.) are firstly prepared,[13,21–27,29–41] which is followed by subsequent phase transformation to their pure metal oxide counterparts via various processes such as thermal decomposition, hydrothermal treatment or oxidation/reduction in air or a controlled atmosphere at elevated temperatures. In recent years, in particular, the synthesis of nanostructured Co_3O_4 materials using the solid precursor $Co(CO_3)_{0.5}(OH)\cdot 0.11H_2O$ has also been investigated for different applications.[26,27,42,43] However, the structural organization of this solid compound has not been reported so far, and this solid conversion to cobalt oxides has only focused on the Co_3O_4 spinel phase as the end product.[26,27,42,43] The further development of a rational synthetic strategy for preparing both Co_3O_4 and CoO nanostructures with tunable morphologies appears to remain a challenge for the further development of this preparative route for nanostructured cobalt oxides. Herein, in this article, we describe an original hydrothermal process that we have devised for the shape-controlled synthesis of 1D $Co(CO_3)_{0.5}(OH)\cdot 0.11H_2O$ nanocrystals, where different morphologies are achieved by adjusting the reaction parameters in the presence of sodium chloride. To the best of our knowledge, this uniform, chrysanthemum-like, organized $Co(CO_3)_{0.5}(OH)\cdot 0.11H_2O$, comprising long nanowires, has been prepared for the first time using our hydrothermal process. After a sequential topotactic conversion from $Co(CO_3)_{0.5}(OH)\cdot 0.11H_2O$ in laboratory air or in an acetylene-containing gas stream, quasi-single-crystalline, mesoporous Co_3O_4 nanowire arrays and carbon-decorated CoO (i.e., CoO@C) nanowire arrays were obtained, respectively. Furthermore, the electrochemical performance of both the Co_3O_4 nanowire arrays and the carbon-sheathed CoO nanowire arrays as anode materials for LIBs application were also evaluated, which shows that the CoO@C nanocomposite displays a high reversible capacity of about 800 mA h g^{-1} and an excellent cyclability after prolonged testing.

2. Results and Discussion

2.1. Formation of the $Co(CO_3)_{0.5}(OH)\cdot 0.11H_2O$ Precursors

With our starting chemical precursors, the formation reactions of the $Co(CO_3)_{0.5}(OH)\cdot 0.11H_2O$ phase can be described in the following steps:

$$CO(NH_2)_2 + 3H_2O \rightarrow 2NH_4^+ + CO_2 + 2OH^- \quad (1)$$

$$CO_2 + 2OH^- \rightarrow CO_3^{2-} + H_2O \quad (2)$$

$$Co^{2+} + 0.5CO_3^{2-} + OH^- + 0.11H_2O \rightarrow Co(CO_3)_{0.5}(OH)\cdot 0.11H_2O \quad (3)$$

It should be mentioned that the urea used in the present synthesis mainly serves as a source for the generation of both carbonate and hydroxyl anions, as explained in Equation 1 and Equation 2, while the divalent cobalt cations required in Equation 3 are from cobalt chloride.

Figure 1a gives the X-ray diffraction (XRD) pattern of the cobalt carbonate hydroxide that was prepared through our urea-assisted hydrothermal process with a $CoCl_2$:NaCl:$CO(NH_2)_2$ molar ratio of 0.5:1:1 at 100 °C for 12 h (Experimental Section). All of the diffraction peaks could be indexed perfectly to orthorhombic $Co(CO_3)_{0.5}(OH)\cdot 0.11H_2O$ (a_o = 8.792 Å, b_o = 10.150 Å and c_o = 4.433 Å; JCPDS card No. 048-0083)[26,27,42,43] without any obvious impurity peaks. The morphology of the as-prepared $Co(CO_3)_{0.5}(OH)\cdot 0.11H_2O$ was investigated using field-emission scanning electron microscopy (FE-SEM), and the panoramic view for this solid sample (Figure 1b) reveals a uniform chrysanthemum-like structure, assembled from individual nanowires with lengths of about tens of micrometers and diameters in the range of 50–100 nm. Interestingly, the long nanowires of this flower-like assembly share a common center and extrude outwards along the radial direction. The nanowires were also quite flexible, as shown in their curling appearance in Figure 1c.

The detailed structure and the growth direction of the $Co(CO_3)_{0.5}(OH)\cdot 0.11H_2O$ nanowires were further examined by transmission electron microscopy (TEM)/high-resolution TEM (HR-TEM). The locally magnified TEM image in Figure 1d clearly confirms that these nanowires were indeed projected from the center of the flowers, forming aggregated radial arrays (i.e., petals) especially in the tip regions. Figure 1e shows a high-magnification TEM image of a single nanowire with a diameter of approximately 100 nm. The HR-TEM image in Figure 1f, selected from the area marked by the white frame in Figure 1e, gives two sets of mutually perpendicular lattice fringes. The observed interplanar distances of 0.30 nm and 1.01 nm correspond very well with the (300) and (010) crystal planes of reported orthorhombic $Co(CO_3)_{0.5}(OH)\cdot 0.11H_2O$ (Figure 1a and JCPDS card No. 048-0083). The inset in Figure 1f is the corresponding fast Fourier transform simulated-electron-diffraction (FFT-ED) pattern of the same image region. Therefore, both the HR-TEM and the FFT-ED studies reveal that these nanowires are single-crystalline in nature and their preferential growth is along the [100] direction, the longitudinal axis of the 1D nanostructures in the petals of the flower-like assembly.

The morphology and dimensions of the prepared $Co(CO_3)_{0.5}(OH)\cdot 0.11H_2O$ precursors were found to strongly depend on the reaction conditions, such as the cobalt precursor salts, the molar ratio between NaCl and $CO(NH_2)_2$ and the reaction temperature. For example, with the present preparative method, it was revealed that anions of the cobalt precursor salts determine the final structure of the $Co(CO_3)_{0.5}(OH)\cdot 0.11H_2O$. No uniform chrysanthemum-like structure assembled by ultralong nanowires could be obtained under similar conditions by only replacing $CoCl_2$ with $Co(Ac)_2$ or $Co(NO_3)_2$ (Figure S1–S2, Supporting Information). Apart from the cobalt precursor salts, we found that the presence of NaCl is indispensible in forming the uniform, chrysanthemum-like, organized $Co(CO_3)_{0.5}(OH)\cdot 0.11H_2O$. In the absence of NaCl, $Co(CO_3)_{0.5}(OH)\cdot 0.11H_2O$ hierarchical structures could still be generated, but the chrysanthemum-like, organized, hierarchical structures with ultralong nanowires did not exist at all (Figure S3–S9, Supporting Information). Therefore, NaCl could also provide an additional control over the product morphology. On the basis of all of these investigations, we know that the

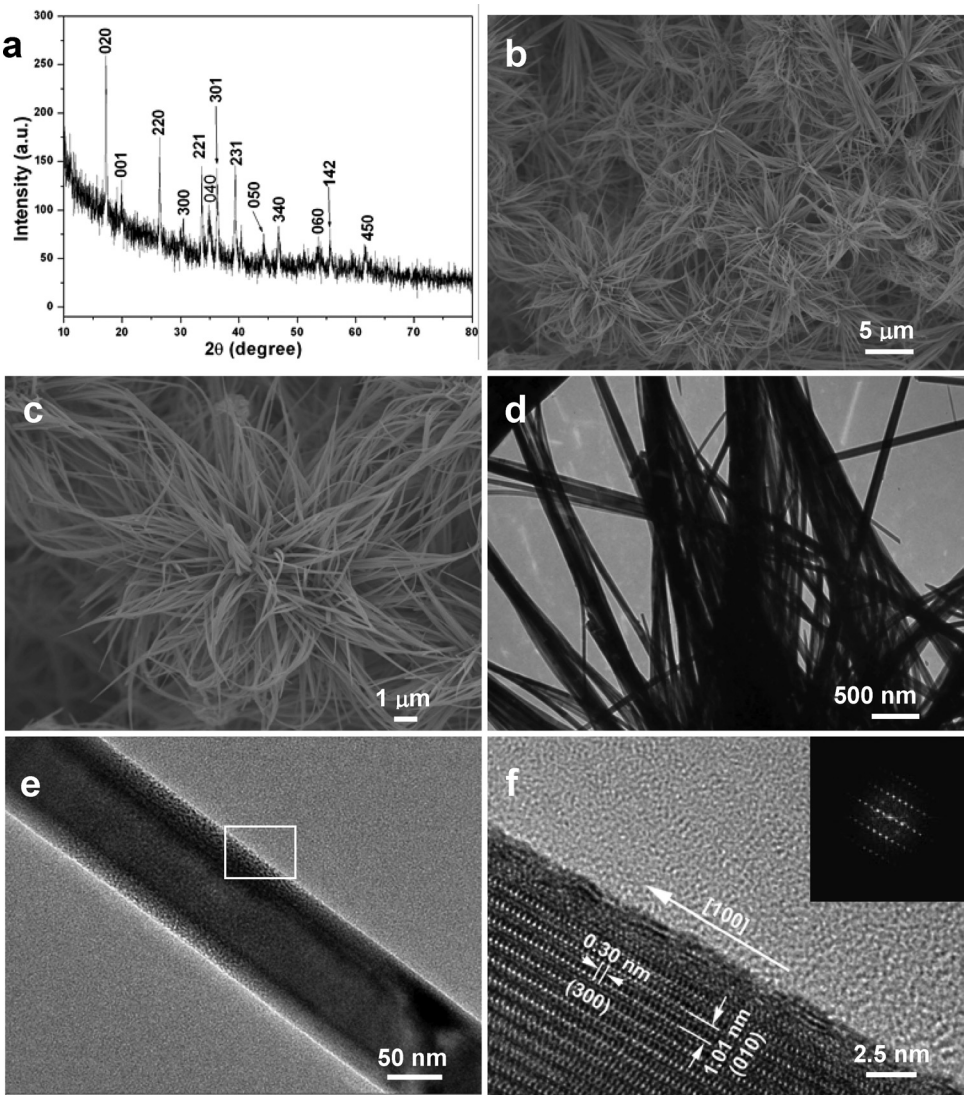

Figure 1. a–c) The XRD pattern (a) and corresponding FE-SEM images at different magnifications (b,c) for the chrysanthemum-like $Co(CO_3)_{0.5}(OH)\cdot 0.11H_2O$ hierarchical microstructures assembled by the nanowires. d) A detailed view of the flower-like hierarchical microstructure (TEM image). e) An individual nanowire of $Co(CO_3)_{0.5}(OH)\cdot 0.11H_2O$ (TEM image). f) An HR-TEM image of lattice fringes for the area marked with a rectangle in Figure 1e. The inset in panel (f) is the corresponding FFT-ED pattern generated from the HR-TEM image.

presence of an appropriate amount of chlorine anions is important to generate the chrysanthemum-like structure. In order to have more understanding of this structural formation in this series of tests, the molar ratio of NaCl to urea was varied in the range of 1:1, 2:1 and 3:1, and, again, the syntheses were all conducted at 100 °C for 12 h. Quite interestingly, the morphologies of the reaction products gradually transformed from flower-like microstructures assembled with long nanowires (Figure 1; $NaCl:CO(NH_2)_2$ = 1:1) to a coexistence of both shuttle-like fusiform bundles and the flower-like assemblies (**Figure 2**a; $NaCl:CO(NH_2)_2$ = 2:1), and, finally, to bundles of nanowires without conjugation, but the radiating trend of the architecture remained (Figure 2b; $NaCl:CO(NH_2)_2$ = 3:1). In addition, we also investigated the effect of reaction temperature on the product morphology. Under the same molar ratio of $NaCl:CO(NH_2)_2$ = 1:1, for example, sisal-like assemblages with straight nanowires were obtained at 180 °C (Figure 2c–d) instead of those obtained at 100 °C (Figure 1). Thus, the morphology of our $Co(CO_3)_{0.5}(OH)\cdot 0.11H_2O$ products can be finely tuned by manipulating the synthetic parameters, such as the molar ratio of NaCl to urea and the reaction temperature.

To get more insight into the actual evolution process of organized $Co(CO_3)_{0.5}(OH)\cdot 0.11H_2O$, a series of time-dependent experiments was conducted, and the intermediate solids at the different reaction stages (nucleation and growth, etc.) were examined. **Figure 3** shows representative TEM images for the samples collected stepwise after 1.5, 2.0, 2.5 and 4.0 h of reaction. These sequential images reveal a morphological evolution from sheet-like aggregates to short, then long nanowires, and finally to the flower-like hierarchical assemblies (for additional time-dependent FE-SEM and XRD data, see Figure S10, Supporting Information). In the initial stage of the hydrothermal

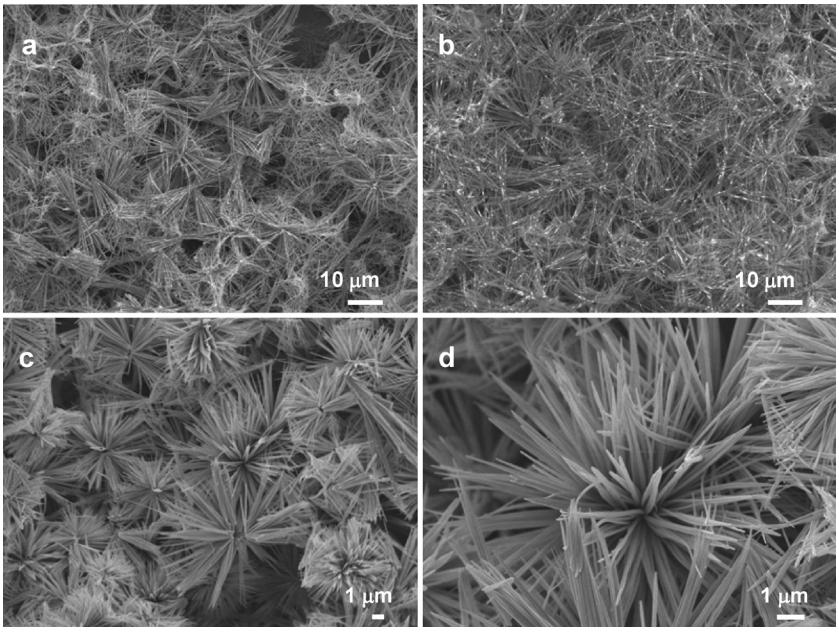

Figure 2. a–d) FE-SEM images of $Co(CO_3)_{0.5}(OH)\cdot 0.11H_2O$ samples prepared at different experimental conditions: molar ratio of NaCl:$CO(NH_2)_2$ = 2:1 at 100 °C for 12 h (a); molar ratio of NaCl:$CO(NH_2)_2$ = 3:1 at 100 °C for 12 h (b); and molar ratio of NaCl:$CO(NH_2)_2$ = 1:1 at 180 °C for 12 h (c,d).

reaction, soft flake-like sheets were formed: the varying dark-image contrasts in the nanoscale dimension represent either the thickness or curling parts of these sheets (Figure 3a). Nonetheless, the nanosheets gradually evolved into curved, interconnected wire structures with diameters in the range of 15–25 nm (Figure 3b). When the reaction time was extended, the unorganized, short wires grew into wires with bigger diameters, and their external surfaces seemed to become much smoother (Figure 3c–d), indicating a recrystallization process taking place and a gain in single-crystallinity for the products. Based on the HR-TEM result in Figure 1f, we know that the $Co(CO_3)_{0.5}(OH)\cdot 0.11H_2O$ nanowires grow preferentially along the [100] direction. Therefore, with the current experimental settings, growth along the other principal crystal directions such as [010] and [001] was retarded, which is key to the formation of latitudinal boundaries of the nanowires. Nevertheless, lateral fusion among the individual nanowires is also quite important for the final flower-like and/or sisal-like organizations. It is clearly indicated that Ostwald ripening plays a pivotal role in the above crystal morphological evolution, although aggregative lateral attachment is also responsible for hierarchical organization in the later stage.

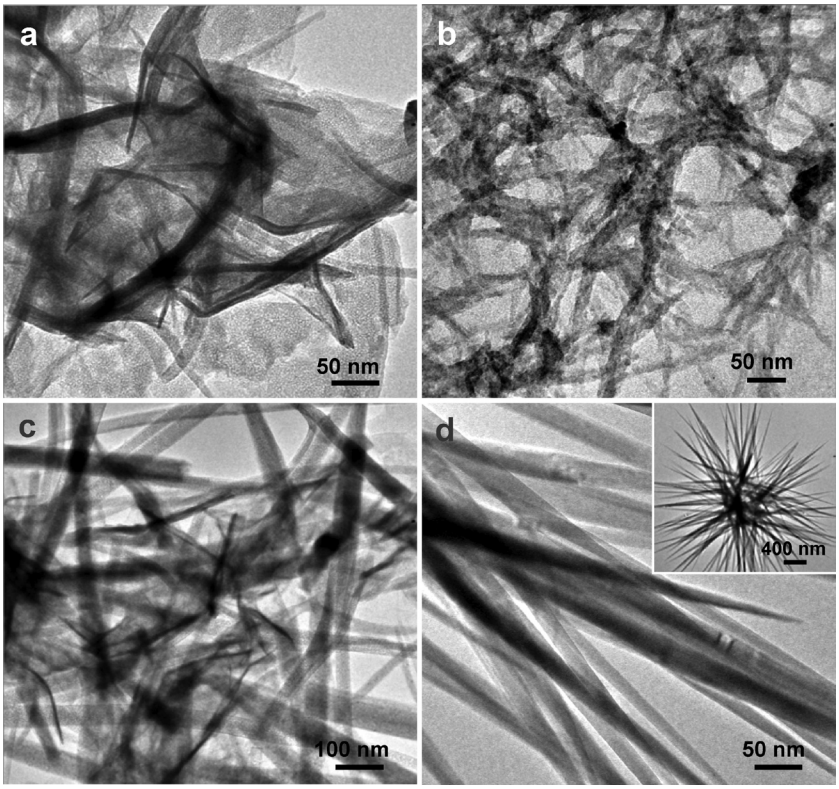

Figure 3. a–d) Structural evolution of the $Co(CO_3)_{0.5}(OH)\cdot 0.11H_2O$, flower-like, hierarchical microstructures prepared at 100 °C after different reaction times (TEM images): 1.5 h (a), 2.0 h (b), 2.5 h (c) and 4.0 h (d). The inset in panel (d) is the panoramic image of an individual flower.

2.2. Transformation of $Co(CO_3)_{0.5}(OH)\cdot 0.11H_2O$ to Co_3O_4 and to CoO@C

In **Figure 4**a, the investigation of the chemical composition and thermal behavior of the $Co(CO_3)_{0.5}(OH)\cdot 0.11H_2O$ nanowires by the thermogravimetric analysis (TGA) is shown. The derivative-TGA (DrTGA) analysis shows that a major thermal event took place at 300 °C during the heating process. Above 300 °C, the total weight loss of the sample is about 24.86%, originating from the decomposition of this solid precursor into Co_3O_4, CO_2 and H_2O in the presence of oxygen in the air stream used in the TGA measurement. This value is lightly smaller than the theoretical value (25.63%) for this thermal decomposition, maybe due to partial loss of H_2O in the crystal structure in the process. For instance, if the dehydrated precursor were considered as being $Co(CO_3)_{0.5}(OH)$, the related theoretical weight loss would then be 24.20%, which is close to the experimental value of 24.86%. The XRD pattern of the as-decomposed product is displayed in Figure 4b(i). All of the diffraction peaks could

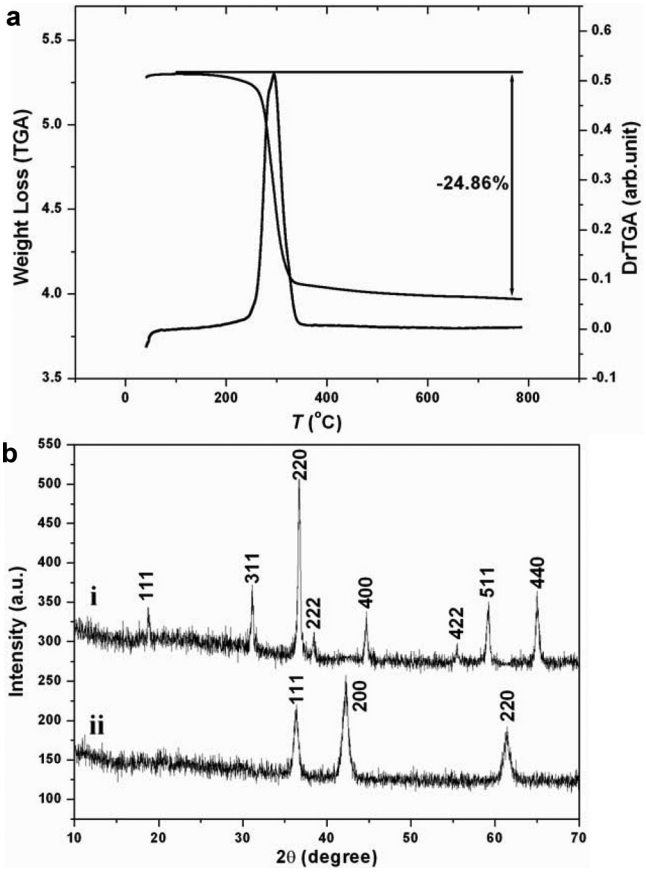

Figure 4. a) TGA and DrTGA curves for the $Co(CO_3)_{0.5}(OH)\bullet 0.11H_2O$ flower-like hierarchical microstructures. b) XRD patterns for the Co_3O_4 nanowire arrays prepared through annealing the $Co(CO_3)_{0.5}(OH)\bullet 0.11H_2O$ flower-like precursor in air at 300 °C for 2 h (i) and for the carbon-decorated CoO nanowire arrays prepared in a horizontal quartz-tube reactor with acetylene/argon as a reducing agent (ii).

be indexed as face-centered-cubic (fcc) Co_3O_4 (a_o = 8.065 Å; space group $Fd\bar{3}m$ (227), JCPDS No. 74-1657). In our preparation of CoO@C nanocomposites, acetylene (C_2H_2) was chosen to serve both as a reducing agent to transform the Co_3O_4 nanowires into the CoO phase and as a carbon source to wrap the resultant CoO nanowires. As expected, the XRD pattern in Figure 4b(ii) indeed demonstrates that the obtained product was fcc CoO (a_o = 4.262 Å; space group $Fm\bar{3}m$ (225), JCPDS card no. 78-0431).

In this work, we also performed an X-ray-photoelectron-spectroscopy (XPS) analysis of both the Co_3O_4 and the CoO@C nanowires, and the results are shown in **Figure 5**. All of the binding energies (BEs) in this XPS analysis were corrected for specimen charging by referencing them to the C 1s peak (set at 284.6 eV). For the Co_3O_4 nanowire arrays in Figure 5a, the Co 2p spectrum shows two major peaks with BE values at 779.7 and 795.2 eV, assigned to the Co $2p_{3/2}$ and Co $2p_{1/2}$ peaks, respectively, with a spin-orbit splitting of 15.5 eV.[44,45] The absence of prominent shake-up satellite peaks in the Co 2p spectra further suggests the formation of the Co_3O_4 phase.[46,47] The deconvoluted O 1s spectrum in Figure 5b displays three photoelectron peaks at 530.0, 531.2 and 532.3 eV that can be assigned to the lattice oxygen in the spinel Co_3O_4, the oxygen in hydroxide ions and the oxygen of surface-adsorbed carbonate anions, respectively. On the other hand, the two Co $2p_{3/2}$ and Co $2p_{1/2}$ peaks located at 780.8 and 796.7 eV in the Co 2p spectrum of Figure 5c are accompanied by two prominent shake-up satellite peaks (786.1 and 802.7 eV) which distinctly verify the presence of the CoO phase.[28] Similar to those in Figure 5b, the peaks at 529.9 and 531.7 eV in the O 1s spectrum of Figure 5d can be ascribed to the lattice oxygen in the CoO phase and the oxygen of the hydroxide ions, and the peak observed at 533.0 eV to a small amount of physically adsorbed water molecules. On the basis of the above combined XRD/XPS analysis, we now confirm that the Co_3O_4 and CoO are the two prime cobalt oxide phases that existed, respectively, in the thermally decomposed sample and in the C_2H_2-reduced sample.

Further morphological and structural characterizations were carried out using both FE-SEM and TEM (HR-TEM) microscopic methods. **Figure 6**a shows a typical low-magnification FE-SEM image of the Co_3O_4 nanowires, showing a similar 1D morphology to their $Co(CO_3)_{0.5}(OH)\cdot 0.11H_2O$ precursor, except for a rougher exterior. The magnified TEM image in Figure 6b clearly indicates that these nanowires with porous features were constructed from moniliforme-shaped nanoparticles. Figure 6c shows a locally magnified HR-TEM image of a Co_3O_4 nanowire viewed along the [112] direction of the crystal. In view of the commensurate lattice fringes, it is noteworthy to point out that different single-crystalline Co_3O_4 grains were also well interconnected, maintaining the same crystallographic orientation, which is a typical feature of mesocrystals within a porous structure. The inset displays the corresponding FFT-ED pattern with clear diffraction spots, further demonstrating the highly oriented growth of Co_3O_4 nanocrystals within the precursor matrix of the single-crystalline $Co(CO_3)_{0.5}(OH)\cdot 0.11H_2O$ nanowires (Figure S11, Supporting Information). After calcination of the Co_3O_4 nanowires in the presence of C_2H_2 at 400 °C, carbon-capped CoO nanocomposites were produced. As shown in Figure 6d, the nanowire morphology was also preserved after the carbonization heat treatment. A careful comparison of Figure 6a with Figure 6d reveals that the surfaces of CoO@C were much smoother, owing to the deposition of the carbon skins. Figure 6e shows an HR-TEM image of an individual carbon-capped CoO nanowire, from which it can be seen that a thin amorphous carbon coating was successfully deposited at a thickness of only about 5–14 nm (see also Figure S12, Supporting Information). The HR-TEM image of Figure 6f exhibits a large area of coherent lattice fringes around a large pore (marked by the circle in Figure 6e), although there are some plane-stacking faults. The (–111) crystal plane of the CoO phase (d_{-111} = 0.25 nm), which is parallel to the nanowire growth direction, is also observable. Together with the FFT-ED result (in the inset) and in comparison with those in Figure 6c, it could thus be deduced that the CoO nanowires were essentially single-crystalline and they had grown along the [110] axis of the crystal.

From the viewpoint of crystal-lattice matching, a topotactic phase transformation for the material preparation can be further proposed. It was recognized that the (300), (220) and (110) crystal planes of the three samples were all normal to their growth directions (marked with white arrows in Figure 1

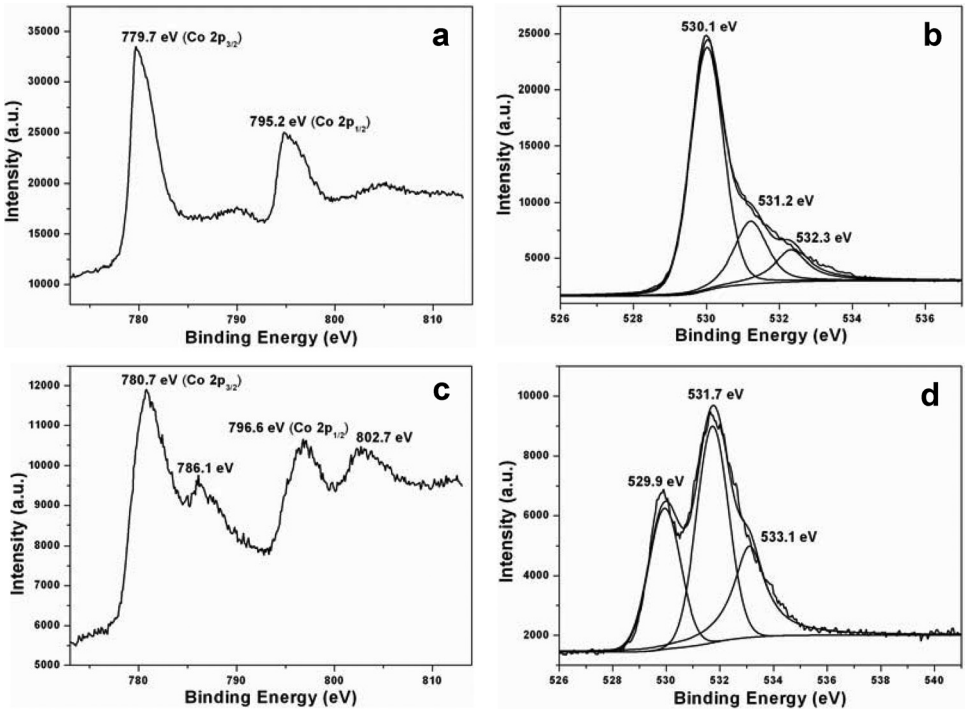

Figure 5. a–d) XPS spectra of Co_3O_4 nanowire arrays (a,b) and carbon-decorated CoO nanowire arrays (c,d). Also refer to Figure 4b.

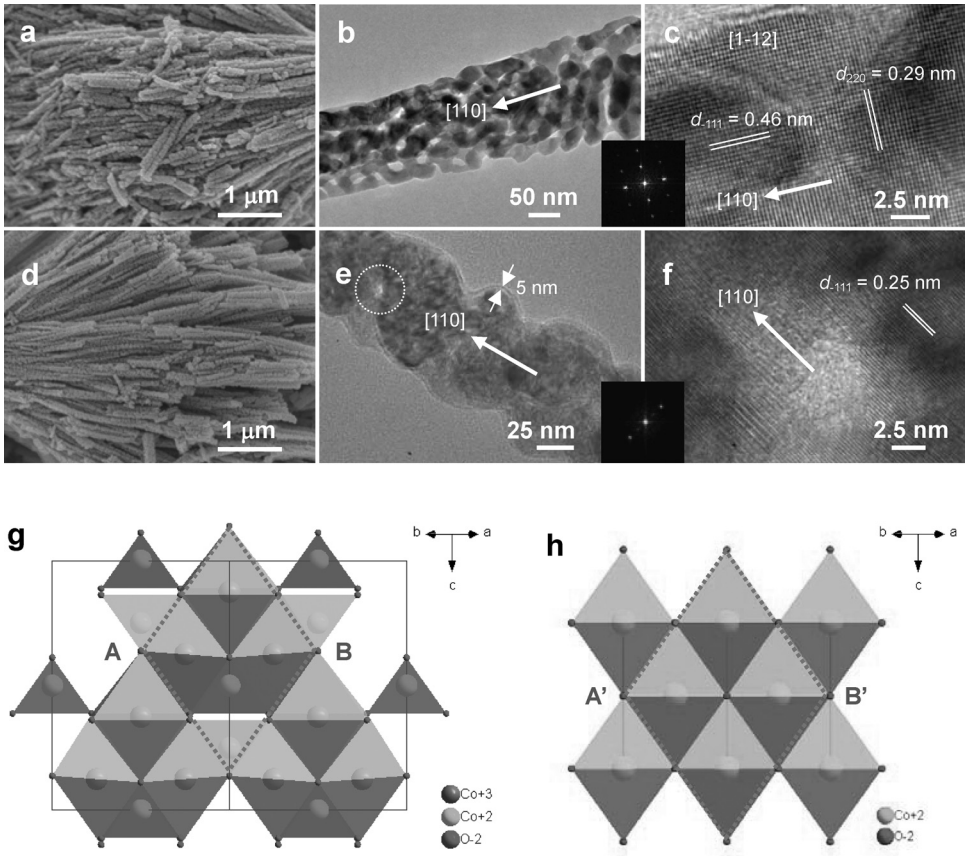

Figure 6. a–f) Morphological and structural characterization of Co_3O_4 and CoO: FE-SEM images of as-synthesized Co_3O_4 nanowires and carbon-decorated CoO nanowires (CoO@C) (a,d); TEM and HR-TEM images of a mesocrystalline Co_3O_4 nanowire (b,c); and TEM and HR-TEM images of a mesocrystalline, carbon-decorated CoO nanowire (CoO@C) (e,f). The insets are the corresponding FFT-ED patterns generated from Figure 6c and Figure 6f. g–h) Structural illustrations viewed along [110] direction are depicted for the Co_3O_4 (g) and CoO (h) phases, respectively.

and Figure 6), and the interplane distances were 2.93 Å (d_{300}, $Co(CO_3)_{0.5}(OH)\cdot 0.11H_2O$), 2.85 Å ($d_{220}$, Co_3O_4) and 3.01 Å (d_{110}, CoO) respectively. On the other hand, the respective crystal planes (040), (222) and (111) were all parallel to the growth directions; the interplane distances were 2.53 Å (d_{040}, $Co(CO_3)_{0.5}(OH)\cdot 0.11H_2O$), 2.33 Å ($d_{222}$, Co_3O_4) and 2.46 Å (d_{111}, CoO). These interplane distances match each other very well, and this may underlie the observed structural conversions. In Figure 6g–h, we depict two schematic structures of the (110) crystal planes of the Co_3O_4 and CoO phases (see Figure S13, Supporting Information, for the structural projection along the [001] axis). For the Co_3O_4 spinel lattice, the Co(II) cations are homed in tetrahedral sites formed by four oxygen anions, while the Co(III) cations are located in octahedral sites by six oxygen anions. For the CoO structure, the Co(II) cations are all present in the rock-salt-like octahedral sites built from oxygen anions. In principle, the transformation process from Co_3O_4 to CoO must be related to the structural relationships between the tetrahedral and octahedral oxygen anions upon a reductive change from trivalent to divalent cobalt cations. From the structural projections (Figure 6g–h), therefore, it can be speculated that two neighboring oxygen tetrahedra of Co_3O_4 combine into one octahedron of CoO through a minimum ion rearrangement, as shown in the rhombic framework defined by the dotted lines. The crystallographic parameters of the two cobalt oxides, in fact, further support this postulation. The length AB of the fcc Co_3O_4 is 5.703 Å (at $a_o(Co_3O_4) = 8.065$ Å), and the distance A′B′ of the fcc CoO has a length of 6.027 Å (at $a_o(CoO) = 4.262$ Å), rightly consistent with the face diagonal line. Because both the metal oxides are closest packed in the lattice oxygen, the spatial matching ratio of AB and A′B′ reaches as high as 94.3% (Figure 6g–h), naturally favorable for the recombination of two adjacent tetrahedra of Co_3O_4 into one octahedron of CoO and hence a reductive topotactic transformation may explain the easy formation of the CoO well, under the reducing atmosphere of C_2H_2:

$$Co_3O_4 + C_2H_2 \rightarrow 3CoO + 2C + H_2O \quad (4)$$

Note that the resultant carbon deposition was accumulated on the surface of CoO crystallites, giving rise to the generation of the CoO@C nanocomposites.

The above topotactic transformation was also confirmed in our HR-TEM results. For example, the crystal-growth orientation of a porous Co_3O_4 nanowire was grown along the [110] direction ($d_{220} = 0.29$ nm, Figure 6c), which was indeed parallel to that observed in the growth direction [100] of its precursor $Co(CO_3)_{0.5}(OH)\cdot 0.11H_2O$ nanowire ($d_{300} = 0.30$ nm, Figure 1f), noting that the two *d*-spacing values are almost identical. In this agreement, similarly, both $d_{111}(Co_3O_4)$ and $d_{111}(CoO)$ can be observed in parallel to the growth directions of the two types of oxide nanowires (Figure 6c versus Figure 6f), noting that $d_{222}(Co_3O_4)$ and $d_{111}(CoO)$ are also quite similar (i.e., $½d_{111}(Co_3O_4) = d_{222}(Co_3O_4) \approx d_{111}(CoO)$), as discussed earlier.

2.3. Textural Characteristics and Electrochemical Properties

To further investigate the specific surface areas and the porous nature of the Co_3O_4 and the carbon-decorated CoO nanowires (i.e., CoO@C), Brunauer–Emmett–Teller (BET) gas-sorption measurements were performed.[48] The N_2 adsorption-desorption isotherms at 77 K are reported in **Figure 7**, with the insets showing their corresponding Barrett–Joyner–Halenda (BJH) pore-size distribution.[48] The isotherms of the Co_3O_4 powers prepared at 400 °C (S-1, Figure 7a) and 350 °C (S-2, Figure 7b) can be classified as type IV,[48] having a distinct hysteresis loop at relative pressure ranges of 0.83–1.0 and 0.77–1.0 P/P_0, respectively. Their BET specific surface areas are about 20.2 and 19.8 $m^2\ g^{-1}$, respectively. By comparing the isotherms and pore-size distributions of S-1 and S-2, it is clear that the relative pressure was enhanced with increasing heat-treatment temperature, showing the decreasing pore sizes and the loss of larger pores. This may demonstrate that, at higher temperature, the Co_3O_4 nanowires are arranged more compactly, resulting in smaller pores. However, the isotherm of the carbon-decorated CoO nanowires (S-3, Figure 7c) shows a wide hysteresis loop at a relative pressure range of 0.4–1.0 P/P_0 and the corresponding BET specific surface area is 30.1 $m^2\ g^{-1}$. The higher surface area of the carbon-decorated CoO nanowires may also be attributable to the presence of a thin carbon layer around the CoO nanowire arrays, apart from the intrinsic pores of CoO phase. The BJH pore-size-distribution curves of Figure 7 indicate that most of the pores were around 8, 12 and 10 nm for the S-1, S-2 and S-3 samples, respectively.

Since it is known that nanosized transition-metal oxides can serve as negative electrode materials for LIBs,[49] nanostructured cobalt oxides have received considerable research attention over the past decade. Herein, to evaluate the electrochemical properties of our cobalt oxide-based nanostructures for LIB applications, galvanostatic discharge-charge and cycling measurements were conducted at room temperature and at current densities of 50 and 100 mA g^{-1} in the voltage window of 0.01–3.0 V. The relevant results are presented in **Figure 8**. The first discharge curves in Figure 8a for S-1 and S-2 show similar electrochemical behaviors and can be divided into two voltage ranges. On the one hand, in the higher-voltage region, two well-defined voltage plateaus at around 1.2 and 1.05 V can be observed. These are generally attributed to the conversion from Co_3O_4 to an intermediate-phase CoO (or $Li_xCo_3O_4$) and then to metallic Co, respectively.[49,50] On the other hand, the lower-voltage curves slip down to 0.01 V. In general, the occurrence of a high-voltage plateau is relatively rare, and has previously only benn observed for nanotextured Co_3O_4 with a high surface area or a very-low current density.[15,25,50] For the reactivity mechanism of Li^+ with cobalt oxide–metal system, the involved reversible reaction mechanism during charging (left to right)/discharging (right to left) can be expressed as follows:[49,50]

$$Co_3O_4 + 8Li^+ + 8e^- \rightleftharpoons 3Co^0 + 4Li_2O \quad (5)$$

$$CoO + 2Li^+ + 2e^- \rightleftharpoons Co^0 + Li_2O \quad (6)$$

As shown in Figure 8a, the initial discharge capacities were 1732, 1866 and 1564 mA h g^{-1} for the S-1, S-2 and S-3 samples, respectively, which are all much larger than the theoretical capacity of bulk Co_3O_4 (892 mA h g^{-1}; the theoretical

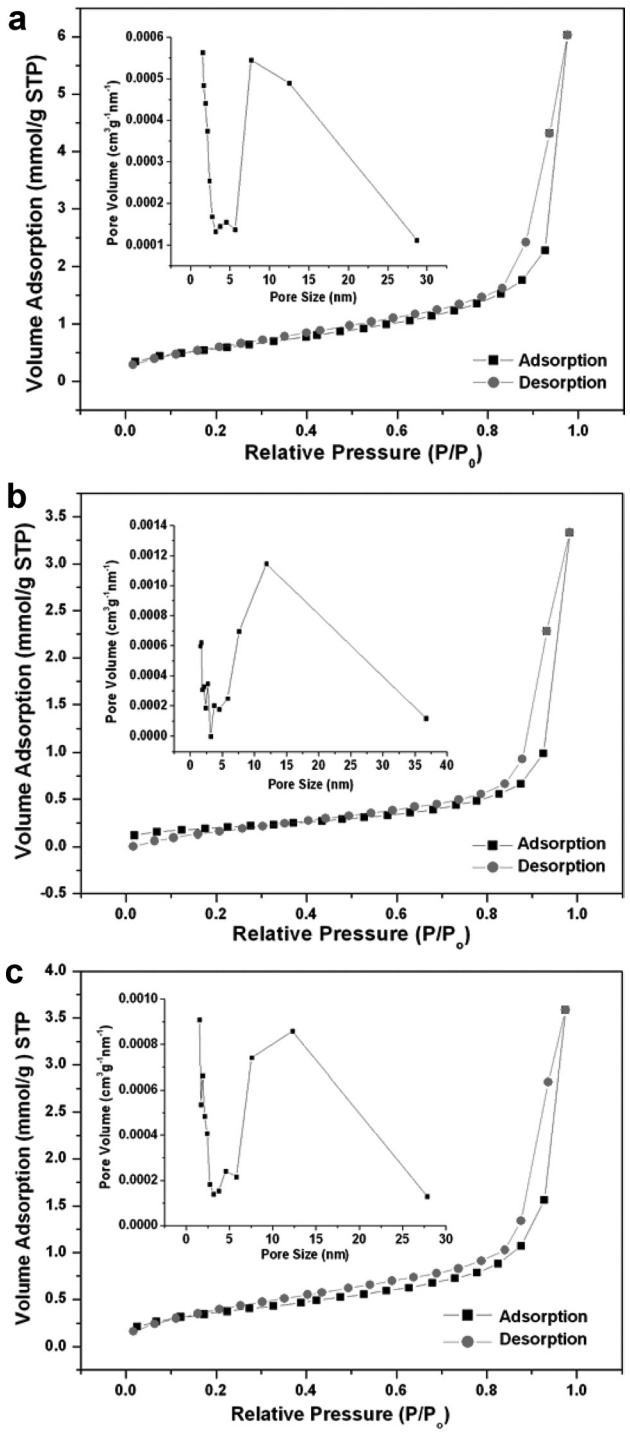

Figure 7. a–c) Nitrogen adsorption-desorption isotherms and pore-size-distribution curves (insets) of: Co_3O_4 nanowire arrays produced at 400 °C (denoted as S-1) (a); Co_3O_4 nanowire arrays produced at 350 °C (denoted as S-2) (b); and carbon-decorated CoO (CoO@C) formed from Co_3O_4 nanowire arrays at 400 °C with a gas stream of C_2H_2 and Ar (denoted as S-3) (c).

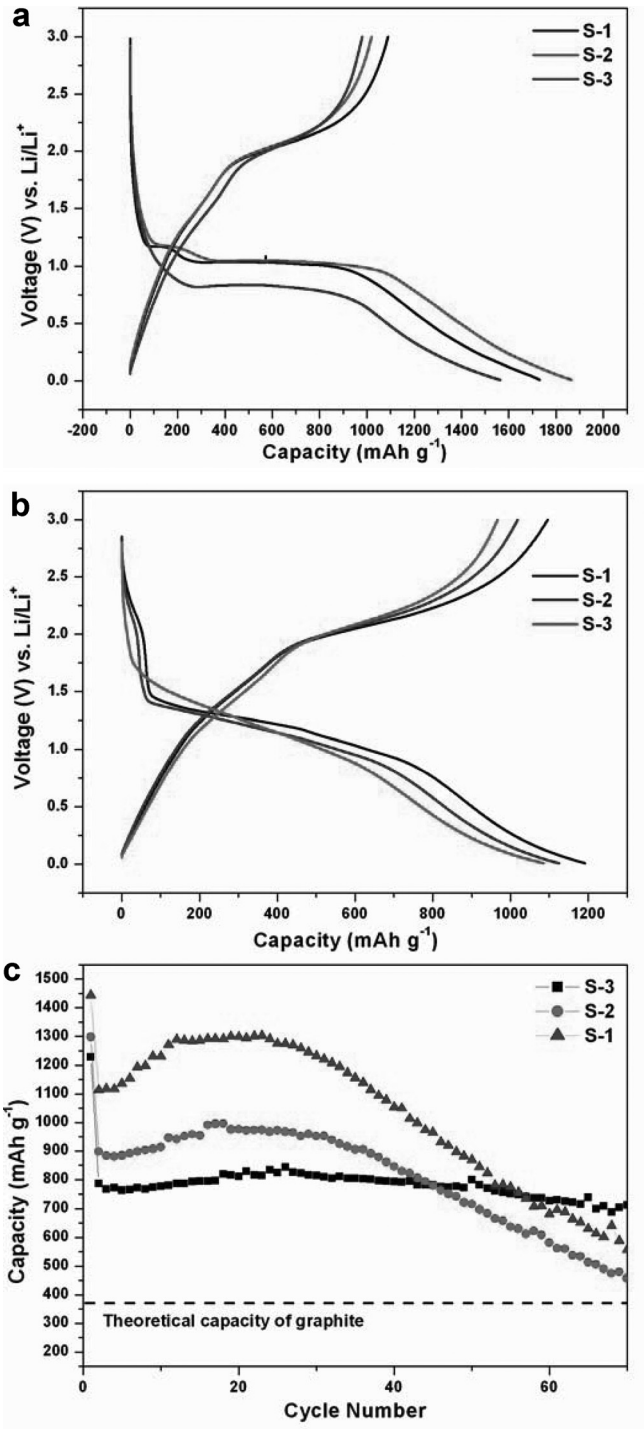

Figure 8. a–b) First (a) and second (b) charge/discharge curves in the voltage range of 0.01–3.0 V at a current rate of 50 mA g^{-1}. c) Cyclic performance of electrodes prepared from the Co_3O_4 samples (S-1 and S-2, Figure 7) and the carbon-decorated CoO sample (S-3, Figure 7) in the voltage range of 0.01–3.0 V at a current density of 100 mA g^{-1}.

capacity of bulk CoO is about 716 mA h g^{-1}). The observed extra capacities are probably attributable to the formation of a solid-electrolyte-interface (SEI) layer due to the irreversible degradation of electrolyte and other secondary reactions, as proposed in the literature.[28,51,52] The first charge process of the S-1 sample delivered a lower capacity of 1081 mA h g^{-1} than the first discharge, showing an irreversible capacity shift of 651 mA h g^{-1} with a Coulombic efficiency of 62.4%. During the

second charge/discharge cycle of the S-1 sample, a discharge capacity of 1195 mA h g^{-1} and a charge capacity of 1095 mA h g^{-1} were exhibited, together with an increased Coulombic efficiency to 91.6% (see Figure 8b). The large, irreversible capacity loss (ICL) arising during the first cycle is likely to be due to the incomplete decomposition of Li_2O and the difficult dissolution of the SEI, as well as other factors, such as the intrinsic nature of the materials and kinetic limitations.

As shown in Figure 8c, after the first discharge/charge cycle for all of the samples, the capacities of subsequent cycles were basically retained up to 40 cycles. It is obvious that the S-1 sample was superior, with the highest lithium-storage capacity. Its reversible capacity after 30 cycles was observed at 1240 mA h g^{-1}. This performance is much better than those realized from other materials reported previously.[15,17,22,49] Interestingly, we note that the S-1 sample possessed a specific surface area of 20.2 $m^2 g^{-1}$, which is similar to that of the S-2 sample (19.8 $m^2 g^{-1}$), but the capacity of the S-1 sample (Figure 8c) was much larger than that of the latter, suggesting that the electrochemical performance of the Co_3O_4 nanowire arrays is associated more directly with its structural aspects than its specific surface area; that is to say, the relatively appropriate pore size and surface texture are more convenient and accessible for electrolyte diffusion and intercalation of Li^+ ions into the active phases. Due to the further decrease in the exchange resistance of the Li^+ ions between the electrolyte and the active phases, the charge/discharge performance of the as-synthesized samples was improved. However, without a protective surface graphitic layer, the cyclic performance deteriorated in the S-1 and S-2 samples after 40 cycles. As the measurement time was extended, understandably, the porous structures were subject to volume expansion and structural-framework collapse during the multiple-Li^+-ion insertions and desertions, causing the capacity to slide gradually.

In comparison with the above two samples (S-1 and S-2), from the second cycle onwards, the S-3 sample gave a more-stable capacity at around 800 mA h g^{-1} and showed good cyclic retention during the 70 charge-discharge cycles (Figure 8c). At the beginning, the capacity had a tendency to rise, which may imply that more diffusion paths were created through the amorphous carbon coating on the CoO and/or an induced activation of the CoO phase had taken place. The enhanced cycling performance of the carbon-decorated CoO was attributed to the presence of the thin carbon layer around the CoO nanowire arrays, which prevents adjacent nanowires from contacting each other directly and therefore minimizes the aggregation of the nanowires in the charge/discharge processes. In addition, the nanocarbon sheath also furnishes an elastic inactive matrix that can buffer the massive volume expansion and contraction occurring during the repeated electrochemical reactions. Apart from the easy ionic transportation in the nanostructured cobalt oxides, one important factor contributing to the observed excellent LIB performance is that the formation of crystallographically oriented mesocrystals in the active cobalt oxides (Figure 6) may enhance the required charge transfer and thus the electron conductivity during LIB operation, because fewer crystallite boundaries amongst the highly aligned mesocrystals are observed in these porous cobalt oxide products.

3. Conclusions

In summary, we have devised a novel sodium chloride-assisted hydrothermal route to prepare cobalt carbonate hydroxide $Co(CO_3)_{0.5}(OH)\cdot 0.11H_2O$ hierarchical microstructures that are assembled from smaller building units of single-crystalline nanowires. The effects of the synthetic conditions, including the molar ratio of the starting chemicals, any additives, the reaction time and the temperature, on the morphology of the precursor have been investigated in detail. With this synthetic route, the $Co(CO_3)_{0.5}(OH)\cdot 0.11H_2O$ compound was actually obtained through a gradual morphological evolution from flexible nanosheets to random nanowires, and, finally, to chrysanthemum-like nanowire arrays, during which Ostwald ripening played an important role in the structural development. Using this solid precursor, we have also successfully prepared quasi-single-crystalline mesoporous Co_3O_4 nanowire arrays via direct thermal decomposition in laboratory air at temperatures of 300–400 °C. Under the reducing ambience of C_2H_2, furthermore, the as-prepared Co_3O_4 nanowire arrays have been converted into carbon-sheathed CoO nanowire arrays (CoO@C nanocomposites) at 400 °C. A topochemical growth has been proposed to explain the $Co(CO_3)_{0.5}(OH)\cdot 0.11H_2O \rightarrow Co_3O_4 \rightarrow$ CoO@C transformation process, considering the good lattice compatibility among the different solid phases. When examined as the anode material for lithium-ion-battery applications, the as-synthesized Co_3O_4 nanowire arrays showed an enhanced lithium-storage capacity. Our experimental results indicate that the surface texture and pore size are more important than the specific surface area in determining the final performance of the Co_3O_4 nanowire arrays since they can ease ionic transportation in nanostructured materials. The generation of crystallographically oriented mesocrystals in the active cobalt oxide phases may also contribute to charge transfer and hence electron conductivity during battery operation because of the fewer crystallite boundaries present amongst the highly aligned mesocrystals. In addition, the carbon-sheathed CoO nanowire arrays manifested an excellent cyclic performance, with nearly 100 % capacity retention in our testing range (70 cycles of charge/discharge tests). Therefore, the CoO@C nanowire arrays prepared by the present synthetic route might be considered as a potential anode candidate for the future development of lithium-ion batteries.

4. Experimental Section

Chemicals: $CoCl_2\cdot 6H_2O$ (99%, Fluka), $Co(Ac)_2\cdot 4H_2O$ (97%, Nacalai tesque) $Co(NO_3)_2\cdot 6H_2O$ (98%, Sigma–Aldrich), sodium chloride (99.5%, Merck), urea (CH_4N_2O, 99.5%, Fluka) ethanol (C_2H_5OH, absolute for analysis, ACS, Merck) were used. All of the reagents were used as received without further purification.

Preparation of the $Co(CO_3)_{0.5}(OH)\cdot 0.11H_2O$ Precursor: In this work, we have devised a novel chemical route to synthesize $Co(CO_3)_{0.5}(OH)\cdot 0.11H_2O$ solid compound. In a typical synthesis, for example, 1.0 mmol of $CoCl_2\cdot 2H_2O$ was dissolved into 40 mL of deionized water under magnetic stirring. Then, given amounts of NaCl and urea ($CO(NH_2)_2$) were added to the $CoCl_2$ solution at room temperature. The resultant mixture was continually stirred for 5 min and then transferred to a Teflon lined stainless-steel autoclave (capacity of 60 mL). The

autoclave was sealed and maintained at 100 °C for 12 h. The system was then cooled to ambient temperature naturally. The final product was collected and washed with distilled water and absolute alcohol several times, followed by vacuum-drying. The sample was then ready for further processing and characterization. To investigate the formation mechanism of the $Co(CO_3)_{0.5}(OH)\cdot 0.11H_2O$, synthetic parameters such as shorter reaction times and higher reaction temperatures, etc., were also tested; further details can be found in the related discussion.

Preparation of the Co_3O_4 Hierarchical Nanostructures: Various Co_3O_4 hierarchical nanostructures (nanowires/nanobelts) were prepared by heating the corresponding $Co(CO_3)_{0.5}(OH)\cdot 0.11H_2O$ precursors at 300–400 °C inside an electric furnace for 2 h, followed by a natural cooling to room temperature. The heating ambiance was laboratory air and the heating rates were all set at 1 °C min^{-1}.

Preparation of the CoO@C Nanocomposites: The CoO@C nanocomposites were prepared in a horizontal quartz-tube reactor (inner diameter of 7.0 mm) using acetylene (C_2H_2) diluted with purified argon gas (1/9; v/v). The Co_3O_4 powder sample was heated in an electric furnace to 400 °C at 20 °C min^{-1} and purged with a nitrogen stream, in which the nitrogen was fed as a background gas at a constant feed rate of 60 mL min^{-1} and the carbon-source gas, acetylene/argon, was introduced at a rate of 10 mL min^{-1} when the temperature reached a desired value (mostly at 400 °C). This chemical-vapor-deposition process lasted for about 10 min, after which the C_2H_2/Ar stream was turned off, while the product (Co@C) was still kept inside the nitrogen stream for 30 min. The grey powder product was then collected and stored in a clean glass bottle for later materials characterization.

Instrumentation and Sample Analysis: The crystallographic information of the prepared samples was established by powder XRD (Shimadzu, model XRD-6000, Cu Kα radiation: $\lambda = 1.5406$ Å). FE-SEM equipped with a scanning TEM (STEM) function (JSM-6700F, JEOL) was employed to examine the morphologies of the products. Structural and compositional investigations by TEM and HR-TEM were carried out using JEM-2010 (JEOL) and JEM-2100F (JEOL) instruments, operated with an electron kinetic energy of 200 kV. Surface analysis of the studied samples was performed using XPS (AXIS-HSi, Kratos Analytical). XPS of the studied elements was referenced to the C 1s peak arising from adventitious carbon (its binding energy was set at 284.6 eV). TGA (Shimadzu TGA-50) was also conducted to determine the composition of samples. The TGA measurements were carried out at a heating rate of 10 °C min^{-1} from 50 to 800 °C with an air flow-rate of 100 mL min^{-1}. The measurements of the specific surface area and the analysis of the porosity of the Co_3O_4 and carbon-decorated CoO products (Co@C) were performed through measuring N_2 adsorption-desorption isotherms at 77 K, using a Quantachrome NOVA-3000 system.

Electrochemical Measurements: The electrochemical tests were performed under ambient temperature using two-electrode Swagelok type cells with lithium serving as both the counterelectrode and the reference electrode. The working electrode was composed of 70 wt% active material (e.g., our Co_3O_4 or CoO@C nanowire arrays), 20 wt% conductivity agent (carbon black, Super-P-Li), and 10 wt% binder (poly(vinylidene difluoride) (PVDF), Aldrich). The electrolyte used in the cells was 1.00 M $LiPF_6$ in a 50:50 (w/w) mixture of ethylene carbonate (EC) and diethyl carbonate (DEC). The cell assembly was carried out in an argon-filled glove box with both the moisture and the oxygen content below 1 ppm. Galvanostatic charge/discharge was conducted using a battery tester (NEWAER) with a voltage window of 0.01–3.0 V at a current rate of 50–100 mA g^{-1}.

Supporting Information

Supporting Information is available from the Wiley Online Library or from the author.

Acknowledgements

The authors gratefully acknowledge the financial support of the Ministry of Education, Singapore and King Abdullah University of Science and Technology, Saudi Arabia.

Received: September 15, 2011
Revised: November 1, 2011
Published online: December 21, 2011

[1] A. S. Aricò, P. Bruce, B. Scrosati, J.-M. Tarascon, W. V. Schalkwijk, *Nat. Mater.* **2005**, *4*, 366.
[2] E. Kim, D. Son, T.-G. Kim, J. Cho, B. Park, K.-S. Ryu, S.-H. Chang, *Angew. Chem. Int. Ed.* **2004**, *43*, 5987.
[3] Z. Z. Lin, F. L. Jiang, L. Chen, C. Y. Yue, D. Q. Yuan, A. J. Lan, M. C. Hong, *Cryst. Growth Design* **2007**, *7*, 1712.
[4] Y. Wan, D. Y. Zhao, *Chem. Rev.* **2007**, *107*, 2821.
[5] Q. R. Zhao, Z. G. Zhang, T. Dong, Y. Xie, *J. Phys. Chem. B* **2006**, *110*, 15152.
[6] M. E. Davis, *Nature* **2002**, *417*, 813.
[7] A. Gulino, G. Fiorito, I. Fragalá, *J. Mater. Chem.* **2003**, *13*, 861.
[8] A.-M. Cao, J.-S. Hu, H.-P. Liang, W.-G. Song, L.-J. Wan, X.-L. He, X.-G. Gao, S.-H. Xia, *J. Phys. Chem. B* **2006**, *110*, 15858.
[9] C. C. Li, X. M. Yin, T. H. Wang, H. C. Zeng, *Chem. Mater.* **2009**, *21*, 4984.
[10] T.-L. Lai, Y.-L. Lai, C.-C. Lee, Y.-Y. Shu, C.-B. Wang, *Catal. Today* **2008**, *131*, 105.
[11] M. J. Benitez, O. Petracic, E. L. Salabas, F. Radu, H. Tüysüz, F. Schüth, H. Zabel, *Phys. Rev. Lett.* **2008**, *101*, 7026.
[12] M. Ando, K. Kadono, K. Kamada, K. Ohta, *Thin Solid Films* **2004**, *446*, 271.
[13] S. L. Xiong, C. Z. Yuan, X. G. Zhang, Y. T. Qian, *Chem. Eur. J.* **2009**, *15*, 5320.
[14] Y.-M. Kang, K.-T. Kim, J.-H. Kim, H.-S. Kim, P. S. Lee, J.-Y. Lee, H. K. Liu, S. X. Dou, *J. Power Sources* **2004**, *133*, 252.
[15] W.-Y. Li, L.-N. Xu, J. Chen, *Adv. Funct. Mater.* **2005**, *15*, 851.
[16] G. Binotto, D. Larcher, A. S. Prakash, R. H. Urbina, M. S. Hegde, J.-M. Tarascon, *Chem. Mater.* **2007**, *19*, 3032.
[17] Y. Liu, C. H. Mi, L. H. Su, X. G. Zhang, *Electrochim. Acta* **2008**, *53*, 2507.
[18] F. Cheng, Z. Tao, J. Liang, J. Chen, *Chem. Mater.* **2008**, *20*, 667.
[19] Y. G. Li, B. Tan, Y. Y. Wu, *Nano Lett.* **2008**, *8*, 265.
[20] X. Wang, X.-L. Wu, Y.-G. Guo, Y. T. Zhang, X. Q. Cao, Y. Ma, J. N. Yao, *Adv. Funct. Mater.* **2010**, *20*, 1620.
[21] X. W. Lou, D. Deng, J. Y. Lee, L. A. Archer, *J. Mater. Chem.* **2008**, *18*, 4397.
[22] X. W. Lou, D. Deng, J. Y. Lee, J. Feng, L. A. Archer, *Adv. Mater.* **2008**, *20*, 258.
[23] J. S. Chen, T. Zhu, Q. H. Hu, J. J. Gao, F. B. Su, S. Z. Qiao, X. W. Lou, *ACS Appl. Mater. Interfaces* **2010**, *2*, 3628.
[24] H. Zhang, J. B. Wu, C. X. Zhai, X. Y. Ma, N. Du, J. P. Tu, D. R. Yang, *Nanotechnology* **2008**, *19*, 035711.
[25] L. Tian, H. L. Zou, J. X. Fu, X. F. Yang, Y. Wang, H. L. Guo, X. H. Fu, C. L. Liang, M. M. Wu, P. K. Shen, Q. M. Gao, *Adv. Funct. Mater.* **2010**, *20*, 617.
[26] Y. Wang, H. Xia, L. Lu, J. Y. Lin, *ACS Nano* **2010**, *4*, 4753.
[27] Y. Wang, H. J. Zhang, L. Lu, L. P. Stubbs, C. C. Wong, J. Y. Lin, *ACS Nano* **2010**, *4*, 4753.
[28] S. A. Needham, G. X. Wang, K. Konstantinov, Y. Tournayre, Z. Lao, H. K. Liu, *Electrochem. Solid State Lett.* **2006**, *9*, A315.

[29] C. Nethravathi, S. Sen, N. Ravishankar, M. Rajamathi, C. Pietzonka, B. Harbrecht, *J. Phys. Chem. B* **2005**, *109*, 11468.
[30] Y. S. Ding, L. P. Xu, C. H. Chen, X. F. Shen, S. L. Suib, *J. Phys. Chem. C* **2008**, *112*, 8177.
[31] E. Hosono, S. Fujihara, I. Honma, H. S. Zhou, *J. Mater. Chem.* **2005**, *15*, 1938.
[32] Z. G. Zhao, F. X. Geng, J. B. Bai, H.-M. Cheng. *J. Phys. Chem. C* **2007**, *111*, 3848.
[33] B. Y. Geng, F. M. Zhan, C. H. Fang, N. Yu. *J. Mater. Chem.* **2008**, *18*, 4977.
[34] H.-P. Cong, S.-H. Yu, *Cryst. Growth Design* **2009**, *9*, 210.
[35] H. C. Zeng, Y. Y. Lim, *J. Mater. Res.* **2000**, *15*, 1250.
[36] Z. P. Xu, H. C. Zeng, *Chem. Mater.* **2000**, *12*, 3459.
[37] R. Xu, H. C. Zeng, *J. Phys. Chem. B* **2003**, *107*, 926.
[38] R. Xu, H. C. Zeng, *J. Phys. Chem. B* **2003**, *107*, 12643.
[39] J. Feng, H. C. Zeng, *Chem. Mater.* **2003**, *15*, 2829.
[40] R. Xu, H. C. Zeng, *Langmuir* **2004**, *20*, 9780.
[41] J. Feng, H. C. Zeng, *J. Phys. Chem. B* **2005**, *109*, 17113.
[42] L. H. Hu, Q. Peng, Y. D. Li, *J. Am. Chem. Soc.* **2008**, *130*, 16136.
[43] H. Nguyen, S. A. El-Safty, *J. Phys. Chem. C* **2011**, *115*, 8466.
[44] C. V. Schenck, J. G. Dillard, J. W. Murray, *J. Colloid Interface Sci.* **1983**, *95*, 398.
[45] M. Oku, Y. Sato, *Appl. Surf. Sci.* **1992**, *55*, 37.
[46] T. J. Chuang, C. R. Brundle, D. W. Rice, *Surf. Sci.* **1976**, *59*, 413.
[47] M. A. Langell, M. D. Anderson, G. A. Carson, L. Peng, S. Smith, *Phys. Rev. B: Condens. Matter* **1999**, *59*, 4791.
[48] K. S. W. Sing, D. H. Everett, R. A. W. Haul, L. Moscou, R. A. Pierotti, J. Rouquérol, T. Siemieniewska, *Pure Appl. Chem.* **1985**, *57*, 603.
[49] P. Poizot, S. Laruelle, S. Grugeon, L. Dupont, J.-M. Tarascon, *Nature* **2000**, *407*, 496.
[50] D. Larcher, G. Sudant, J.-B. Leriche, Y. Chabre, J.-M. Tarascon, *J. Electrochem. Soc.* **2002**, *149*, A234.
[51] G. Binotto, D. Larcher, A. S. Prakash, R. H. Urbina, M. S. Hegde, J.-M. Tarascon, *Chem. Mater.* **2007**, *19*, 3032.
[52] S. Laruelle, S. Grugeon, P. Poizot, M. Dollé, L. Dupont, J. M. Tarascon, *J. Electrochem. Soc.* **2002**, *149*, A627.